Materials Today Chemistry 55 (2026) 103770

Contents lists available at ScienceDirect

Materials Today Chemistry

journal homepage: www.journals.elsevier.com/materials-today-chemistry/

Influence of the coordination features of zinc single sites on the reactivity of zinc-based curing activators

Silvia Mostoni [a,*], Paola Milana [a], Lorenzo Alberti [a], Massimiliano D'Arienzo [a], Emanuela Callone [b], Sandra Dirè [b], Antonio Susanna [c], Raffaella Donetti [c], Barbara Di Credico [a], Roberto Scotti [a]

[a] Department of Materials Science, INSTM, University of Milano Bicocca, Via Roberto Cozzi 55, Milano, 20125, Italy
[b] "Klaus Müller" Magnetic Resonance Lab., Department of Industrial Engineering, University of Trento, via Sommarive 9, Trento, 38123, Italy
[c] Pirelli Tyre S.p.A., Viale Sarca, 222, Milano, 20126, Italy

ARTICLE INFO

Keywords:
Activator
ZnO
Single site
Curing
Vulcanization
Rubber nanocomposites

ABSTRACT

The efficiency of the sulfur cross-linking in rubber is enhanced by zinc-based activators. Zn(II) centers are formed by the interaction of microcrystalline ZnO with fatty acids and generate reactive zinc-based organic complexes through the reaction with the accelerator and sulfur. Despite ZnO is the most used industrial activator, several efforts have been made to find more sustainable alternatives, by reducing the zinc content and the zinc leaching during the lifecycle of rubber products. Among them, a promising candidate recently proposed is composed of Zn(II) single sites anchored onto the surface of silica nanoparticles. This material has proven good curing efficiency, thanks to a good zinc reactivity towards the curing agents and high availability to form active Zn(II) complexes. In this context, the present study deeply investigates the reactivity of the Zn(II) single sites by modifying the zinc coordination onto the silica surface, through the introduction of five surface ligands (L) producing Zn-L-SiO_2 curing activators. These were synthesized by using amino, carboxyl and sulfur-based terminated ligands, to promote different coordination geometry in the Zn(II) coordination sphere. This strongly impacts on the reactivity of Zn(II)-based activators tested during the sulfur curing process, paving the way for their fine tailoring.

1. Introduction

Zinc plays a crucial role in the sulfur curing process of rubber, which is employed to enhance its strength, elasticity and durability, together with the addition of reinforcing inorganic fillers [1]. Specifically, it is added in the form of microcrystalline zinc oxide (ZnO), which represents the worldwide most widespread curing activator in the industrial production of rubber, significantly increasing the efficiency of the sulfur cross-linking within rubber and its reaction rate [2–4].

From a mechanistic point of view, its main scope is both to assist the formation of reactive compounds, i.e. active sulfurating agents, in the first stages of the curing process [5–7] and to induce a more favorable shortening of the poly-sulphidic chains towards more cross-linked materials [8]. The first essential step in the curing process is the generation of Zn(II) centers from microcrystalline ZnO, thanks to the complementary usage of a co-activator (i.e. fatty acids as stearic acid, StH) that reacts forming soluble zinc-based coordination complexes [9]. Despite the structure of this Zn-stearate is generally described as a chelated bidentate complex [5,8], several recent studies have proven that this intermediate complex is composed of bridging bidentate stearate ligands coordinating two Zn(II) centers [10,11], responsible for accelerating the cross-linking reaction [12]. This was validated also by studying the interaction of supported ZnO nanoparticles (NPs) over silica particles as double function fillers with StH, which could lead to structurally different intermediate zinc-stearate complexes based on the ZnO morphological and structural properties [13]. After this first step, these complexes are claimed to interact with the accelerator (i.e. organic species such as benzothiazoles, sulfenamides, thiurams, etc.), forming the active accelerator complexes, where Zn is coordinated to the organic pendants due to the accelerator break, such as mercaptobenzothiazole (MBT) groups [6,14]. The presence of zinc is then reported to facilitate the sulfur insertion in the active accelerator complex to form the active sulfurating agents [5]. The structure of these latter agents has been suggested to include Zn(II) in the poly-sulfidic chain through either a

* Corresponding author.
E-mail address: silvia.mostoni@unimib.it (S. Mostoni).

https://doi.org/10.1016/j.mtchem.2026.103770
Received 16 August 2025; Received in revised form 1 April 2026; Accepted 5 June 2026
Available online 22 June 2026

covalent bond or a coordinative bond between Zn(II) and sulfur [4]. In both cases the stability of the zinc complex could be potentially increased by other ligands such as amino or carboxylate groups, released from the accelerator or the StH [8]. Overall, the debate on the structure and nature of the Zn-complexes formed at all the reaction stages is still open; however, their pivotal role and especially the role of Zn(II) centers in the reaction mechanism and in the enhancement of curing efficiency is undeniable and is supported by the entirety of the current literature [1,5,8,15].

Based on this background and owing to the potentially negative impact on the aquatic systems of the Zn(II) released into the environment during the rubber products life cycle [16–20], the development of new activators as efficient substitutes to ZnO appears challenging and requires a deep knowledge of the zinc coordination chemistry. The possibility to introduce Zn(II) complexes in the reaction, as dithiocarbamate (Zn-DTC), Zn-MBT, acetylacetonate (Zn-AAC), or other green ligand additives based on natural oils or waste recovery materials was recently explored [21–25]. Among them, an interesting study by Przybyszewska et al. [26] demonstrated that the increase of the stability of the zinc complexes results in a lower tendency of Zn(II) to interact with the curing agents. Besides, the size reduction of the Zn-based materials was exploited as a promising tool to increase the exposed area and the reactivity, by introducing nanosized ZnO particles [27–31] as well as supported/dispersed ZnO NPs onto suitable supports [32–37]. In addition, a reduction up to the atomic scale was recently proposed to further enhance the Zn(II) reactivity in the curing process, in line with the increasingly widespread single-atom catalysts in the broad field of heterogeneous catalysis [38–40]. In this context, our group recently proposed an innovative activator in which Zn(II) single-sites were dispersed onto the surface of silica filler NPs (Zn–SiO_2) by means of a surface amino-based ligand [41]. This material already demonstrated higher vulcanization efficiency leading to enhanced mechanical properties and cross-linking densities when compared to a conventional silica filled composite vulcanized with ZnO [41–43]. In this case, the peculiarity is that the isolated Zn(II) centers directly react with the accelerator and sulfur, without any intermediate reaction with the co-activator. However, the design of the Zn(II) single sites requires a careful selection of the coordination groups on the surface ligand chain, as the resultant Zn (II) complexes should be stable enough to form but should show a high reactivity towards the curing agents. This strongly depends on the amount as well as on the coordination mode of the Zn(II) sites on the silica surface, that both determine their stability and reactivity in the curing process.

In this scenario, the aim of this work was to investigate the potential modulation of the reactivity of Zn(II) single sites in the curing process, by a fine tailoring of the Zn(II) coordination over the silica surface. Five surface functionalizing agents (L), having different terminal groups available for Zn(II) anchoring, i.e. amino, carboxyl or sulfur-based ligands, were selected in order to produce Zn-L-SiO_2 curing activators, having both the modified structural and electronic properties of the Zn (II) coordination sphere. Besides, ligands with numerous heteroatoms were considered to promote Zn(II) chelated coordination and analyze the impact on their subsequent reactivity. The materials were *i)* synthesized and fully characterized to get insights into the possible coordination geometry of Zn(II) centers in the presence of various ligands, and *ii)* tested as activators for the curing process of isoprene rubber (IR) nanocomposites (NCs) filled with silica and the resulting mechanical properties preliminary tested. The results highlight that the use of different surface functionalizing ligands is an efficient tool to tune the coordination sphere of Zn(II) single site and represents a promising way to modulate their reactivity in the rubber vulcanization process.

2. Experimental

2.1. Materials

Zn-L-SiO_2 preparation: precipitated silica Rhodia Zeosil MP1165 (BET specific surface area SSA = 160 $m^2\ g^{-1}$) was obtained from Rhodia; (3-Aminopropyl)triethoxysilane, $H_2N(CH_2)_3Si(OC_2H_5)_3$ (99 %, APTES), N-[3-(trimethoxysilyl)propyl]ethylendiamine, $(CH_3O)_3Si(CH_2)_3NHCH_2CH_2NH_2$ (97 %, EDTMS), 3-mercaptopropyl)trimethoxysilane, $HS(CH_2)_3Si(OC_2H_5)_3$ (95 %, MPTMS); ammonium hydroxide, NH_4OH (25 %) and copper nitrate trihydrate $Cu(NO_3)_2 \cdot 3H_2O$ (puriss) were purchased from Sigma Aldrich; succinic anhydride (99 %, SA), carbon disulfide (99.9 %, CDS), triethylamine (99 %, TEA), toluene (99 %), sodium hydroxide pellets NaOH (98 %) and zinc nitrate hexahydrate $Zn(NO_3)_2 \bullet 6H_2O$ (98 %) were obtained from Alfa Aesar; ethanol EtOH (puriss, p.a., absolute, ≥99.8 %) was obtained from Exacta + Optech Labcenter.

For rubber compounding: *cis*-1,4-polyisoprene rubber (IR) from Nizhnekamskneftechim Expor; bis(3-triethoxysilylpropyl) disulfide (TESPD) from Aldrich; antioxidant N-(1,3-dimethylbutyl)-N'-phenyl-p-phenylenediamine 6PPD Santoflex (6PPD) from Flexsys; stearic acid (StH) Stearina TP8 from Undesa; N-cyclohexyl-2-benzothiazole sulfenamide (CBS) Vulkacit CZ/C from Lanxess; sulfur (S_8) Crystex OT33 from Flexsys; micro-crystalline zinc oxide ZnO (wurtzite BET specific surface area = 5 $m^2\ g^{-1}$) from Zincol Ossidi.

2.2. Synthesis of Zn-L-SiO_2 curing activators

Zn-L-SiO_2 NPs were prepared by a two-step procedure (Fig. 1): i) functionalization of SiO_2 NPs with different ligand groups (L-SiO_2), through hydrolysis and condensation of L-terminated silane precursors with the SiO_2 surface hydroxyl groups; ii) addition of the zinc precursor

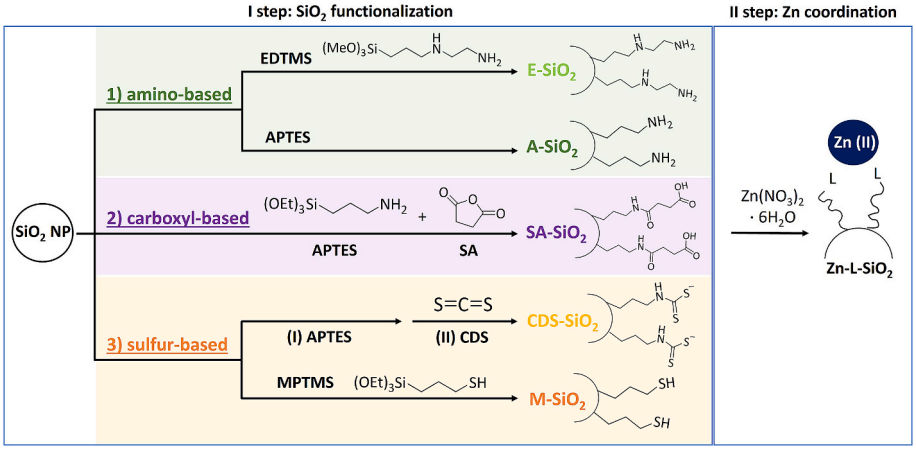

Fig. 1. Scheme of the reaction paths for Zn-L-SiO_2 synthesis.

to L-SiO_2 NPs to promote the Zn-L interaction in the final Zn-L-SiO_2 activators. The L-SiO_2 samples consists of amino or ethylendiamino groups (A-SiO_2 or E-SiO_2, respectively), carboxyl (SA-SiO_2), mercapto (M − SiO_2) or dithiocarbamate groups (CDS-SiO_2).

i) Functionalization of SiO_2 NPs

The functionalization with L-terminated silane was performed by using two amounts of surface ligands, corresponding to a molar ratio between L and surface SiO_2 hydroxyl groups (-OH) equal to 1/6 and 1/2. The number of available hydroxyl groups on silica was determined by TGA by Eq. S(1) as reported in Supporting Information (SI) and was equal to 3.93 mmol/g_{SiO2}. Hereafter, the corresponding samples were labelled as $L_{1/6}$-SiO_2 and $L_{1/2}$-SiO_2.

A- and E-SiO_2 were prepared following a previously described procedure [41]. Briefly, suitable amounts of APTES or EDTMS were added to a SiO_2 suspension in toluene at T = 120 °C and kept under stirring for 24 h. The powder is recovered by filtration, washed twice with fresh toluene and dried at 80 °C for 12 h.

SA-SiO_2 and CDS-SiO_2 are prepared by modifying the terminal –NH_2 groups of APTES into –COOH and CS_2 groups, respectively. In the former case, the SA ring opening reaction and the amide formation from NH_2 groups are carried out by adding SA and APTES simultaneously to the SiO_2 suspension (APTES: SA molar ratio 1:1) at the temperature of 60 °C, to avoid the thermal degradation of SA. In the latter case, TEA and CDS (molar ratios APTES: CDS = 1:2; TEA: APTES = 1:2) are added to 24 mL of toluene at room temperature (RT), under stirring for 10 min. Then, 1.0 g of $A_{1/2}$-SiO_2 is added to the solution to promote the nucleophilic attack of NH_2 to CDS and the reaction is kept under stirring for 24 h at RT. In this case, only $A_{1/2}$-SiO_2 was used to optimize the effective number of CS_2 groups on the SiO_2 surface. The powders were recovered by filtration, washed twice with fresh toluene and dried at RT for 12 h. Finally, M − SiO_2 is synthesized by adding MPTMS and NH_4OH (0.4 % vol/vol) to a SiO_2 suspension in EtOH (1.0 g in 25 mL). The mixture is left under stirring at reflux for 24 h, and the final product is separated by filtration, washed twice with fresh EtOH and dried at 80 °C for 12 h.

ii) Zn (II) anchoring on L-SiO_2 NPs

Zn(II) centers were anchored onto L-SiO_2 NPs as reported in Ref. [41], using $Zn(NO_3)_2{\cdot}6H_2O$ as precursor in EtOH at reflux for 2 h. Three Zn:L molar ratios (0.50; 1; 2) were used in the presence of $L_{1/2}$-SiO_2 to verify the influence of the nominal Zn amount on the Zn coordination with L surface ligands. In the case of $L_{1/6}$-SiO_2, only the Zn: L molar ratio of 0.50 was used. For SA-SiO_2, NaOH (molar ratio NaOH: SA = 1:1) was added to promote the deprotonation of –COOH groups and the temperature kept at 60 °C to avoid their thermal degradation. The powders were then separated by vacuum filtration, washed with fresh EtOH and dried at 60 °C for 12 h.

2.3. Characterization of Zn-L-SiO_2 NPs

The effective functionalization of L-SiO_2 was assessed by Fourier Transform Infrared Spectroscopy in the Attenuated Total Reflectance mode (ATR-FTIR), by using a ThermoFisher Scientific Nicolet instrument (4 cm^{-1} resolution spectra, 4000-650 cm^{-1} region, 32 scans). The amount of L units in L-SiO_2 was evaluated by Thermogravimetric Analysis (TGA) with a TGA/DSC1 STARe system (30-1000 °C temperature range, 10 °C min^{-1} heating rate, constant air flow of 50 mL min^{-1}) and calculated from the weight loss of L-SiO_2 in the range 150-1000 °C ($\Delta W_{150\text{-}1000\,°C}$), according to Eqs. S2-S6 in the SI. To confirm TGA quantification, CHNS Elemental Analysis was carried out with an Elementar VarioMICRO analyzer (temperature of combustion column = 1150 °C, reduction column = 850 °C).

The amount of Zn in Zn-L-SiO_2 was measured by Inductively Coupled Plasma Optical Emission Spectroscopy (ICP-OES) analysis using an ICP-OES Optima 7000 DV PerkinElmer instrument. Sample preparation was carried out according to the procedure reported in the SI. To get insights onto Zn(II) distribution, elemental mapping was performed by Energy Dispersive X-Ray Spectrometer (EDX)-equipped Transmission Electron Microscopy (TEM). The instrument used is a JEOL JEM-2100Plus TEM, operating with an acceleration voltage of 200 kV. Samples were prepared according to the procedure in the SI. Structural features were investigated by powder X-Ray Diffraction (XRD) with a Rigaku MiniFlex 600 diffractometer with 0.154 nm Cu Kα radiation. The measurements were performed in the 2θ range 20-70° (2θ step 0.02°, 2° min^{-1} scan rate).

Electron Paramagnetic Resonance spectroscopy (EPR) was performed by introducing Cu(II) as a paramagnetic probe into Zn-$L_{1/2}$-SiO_2 to gain indirect information on the ligands' geometry and availability to coordinate Zn(II) centers. To this purpose, Cu/Zn-L-SiO_2 materials were synthesize by using $Cu(NO_3)_2{\cdot}3H_2O$ as a Cu precursor with a Cu/Zn molar ratio equal to 1/100. The EPR spectra were acquired using a Bruker EMX spectrometer operating at the X-band frequency and equipped with an Oxford cryostat with the following conditions: 130 K, modulation frequency 100 kHz, modulation amplitude 5 G, and microwave power mW. Solid-state nuclear magnetic resonance (SS-NMR) was carried out both on L-SiO_2 and Zn-L-SiO_2 samples by means of a Bruker Advance 400WB spectrometer with a CPMAS dual band probe analyzing both ^{13}C (υ 100.52 MHz, cross-polarization pulse sequence, 3.5 μs π/2, 2 ms contact time, 6.3 μs decoupling length, 4 s recycle delay, and 2k scans) and ^{1}H (υ 400.13 MHz, 5 μs π/2 pulse, 8 s recycle delay, and 32 scans). Samples were packed in 4 mm zirconia rotors, which were spun at 7 and 10 kHz under air flow. Adamantane was used as external secondary reference.

2.4. Rubber compounding

IR was mixed with Zn-L-SiO_2 as filler and curing activator to obtain silica-filled NCs, using a Brabender Plasti-Corder lab station internal mixer (65 mL mixing chamber, 0.6 filling factor, 60 revolutions per minute (rpm) rotor speed. Three steps were employed for the mixing procedure, as reported in the SI. Hereafter, the NCs prepared with Zn-$L_{1/6}$-SiO_2 materials will be called Zn-$L_{1/6}$-SiO_2/IR. Reference ZnO + SiO_2/IR NCs were prepared by using bare SiO_2 filler and microcrystalline ZnO as curing activator at Zn and SiO_2 content equal to Zn-$L_{1/6}$-SiO_2/IR.

Additionally, Zn-$L_{1/2}$-SiO_2/IR NCs at higher Zn content (1.50 phr) and equal SiO_2 content (43.0 phr) were prepared by using Zn-$A_{1/2}$-SiO_2, Zn-$E_{1/2}$-SiO_2 and Zn-$SA_{1/2}$-SiO_2, together with the respective reference ZnO + SiO_2/IR NC at the same zinc and silica contents.

2.5. Characterization of vulcanized IR NCs

Vulcanization curves and dynamic mechanical properties of IR NCs samples were registered with a Rubber Process Analyzer (RPA2000, Alpha Technologies). The vulcanization was performed at 170 °C for 4 min (frequency = 1.670 Hz, angle = 6.980°) and the related curves were obtained by measuring the torque requested to keep the rotor at a constant rate, that depend on the change of viscosity over time due to the cross-linking process.

The dynamic-mechanical properties were studied with a shear stress mode (70 °C, 10 Hz) at angle values in the range of 0-10 %. Specimens were cut with a constant-volume rubber sample cutter (CUTTER 2000, Alpha Technologies), having a 3.4 cm diameter, 0.2 thickness and a weight of 5.0 ± 0.3 g.

Lastly, swelling experiments in toluene were used to calculate the cross-linking densities of Zn-L-SiO_2/IR, according to Eqs. S7-S8 in the SI.

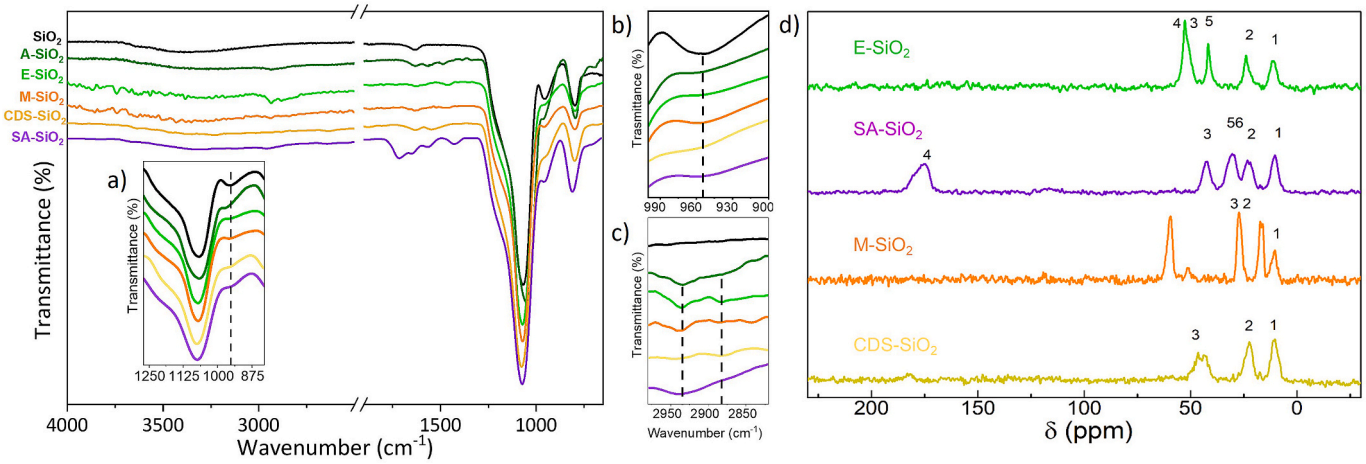

Fig. 2. FTIR (top) and ^{13}C CPMAS NMR (bottom, d) spectra of $L_{1/2}$-SiO_2 compared to bare SiO_2. Magnifications in the wavenumber ranges 1250-850 cm^{-1}, 3000-2800 cm^{-1}, 1800-1400 cm^{-1} are shown in the insets a), b) and c), respectively.

3. Results

3.1. Silica functionalization of L-SiO_2

The functionalization of L-SiO_2 was first investigated through FTIR analysis, by comparing L-SiO_2 spectra to that of bare SiO_2. FTIR spectra of $L_{1/2}$-SiO_2 are shown in Fig. 2, whereas $L_{1/6}$-SiO_2 samples are reported in Fig. S1 and show similar features to $L_{1/2}$-SiO_2 samples.

For all L-SiO_2, the typical peak at 954 cm^{-1} of bare SiO_2, due to the stretching of Si–OH surface groups, enlarges and shifts to higher wavenumbers, probably due to the partial condensation of –OH groups with the alkoxysilanes after SiO_2 functionalization with L groups (Inset a, Fig. 2). Besides, the intensity of the bending peak at 1630 cm^{-1} due to molecular coordinated H_2O adsorbed on bare SiO_2 [44] is partially reduced after functionalization for all L-SiO_2.

The introduction of the silane alkyl chains on the SiO_2 surface is evidenced by the presence of the C–H antisymmetric and symmetric stretching vibrations of the alkyl CH_2 groups at 2934 cm^{-1} and 2880 cm^{-1} (Inset b, Fig. 2). Moreover, in the region 1800-1400 cm^{-1} peaks due to the different functional groups of L can be evidenced (Inset c, Fig. 2). In A-SiO_2 and E-SiO_2 spectra, the peaks at 1570 cm^{-1} and 1490 cm^{-1} correspond to the NH_2 scissoring vibration and the symmetric $-NH_3^+$ bending mode [45], respectively. The corresponding asymmetric mode at 1610 cm^{-1} is not detectable as it overlaps with the intense peak at 1630 cm^{-1}. For E-SiO_2 the additional peak at 1460 cm^{-1}, assigned to the CH_2 bending mode, is more evident due to the longer aliphatic chain compared to APTES.

In SA-SiO_2, the signals at 1701 cm^{-1}, 1650 cm^{-1}, 1562 cm^{-1} and 1430 cm^{-1} are related to the stretching vibration of C=O in terminal COOH groups, the bending vibration of amidic C–N bond formed after APTES-SA interaction and the asymmetric and symmetric stretching of C=O in the amidic unities, respectively. No asymmetric and symmetric stretching peaks at 1789 and 1868 cm^{-1} due to cyclic anhydride groups are detected confirming the complete ring opening of SA after interacting with APTES and the efficient removal of unreacted SA.

No additional peaks related to the sulfur containing groups are detectable in the M – SiO_2 and CDS-SiO_2 spectra, since the spectral feature due to C=S stretching at about 1067 cm^{-1} [46] overlaps with the main SiO_2 signals; besides, the expected weak signal of S–H stretching at ~ 2580 cm^{-1} [46,47] is probably under the detection limit due to its very low amount bonded on the SiO_2 surface, as observed by TGA. However, in the CDS-SiO_2 spectrum, the NH_2 scissoring vibration of APTES shifts at 1555 cm^{-1} and could be related to a modification of the chemical environment of the APTES amine groups after their interaction with CS_2 and C–N bond formation [48].

Overall, the FTIR spectra clearly indicate the presence of organic residues on the SiO_2 NPs for all L ligands. To verify the covalent grafting of these ligands via surface hydroxyl groups, ^{13}C CPMAS NMR spectra were collected for the $L_{1/2}$-SiO_2 series (Fig. 2d), as the higher organic loading provides a better signal-to-noise ratio compared to the $L_{1/6}$-SiO_2 samples. In all spectra, the chemical shift of C1 resonance of the propyl chain (10 ppm) clearly indicates successful silane grafting onto the silica surface, due to the loss of ethoxy and methoxy groups by hydrolysis and condensation reactions [41]. This is confirmed by the almost complete absence of the related methylene and methyl resonances, with the only exception of sample $M_{1/2}$-SiO_2, which exhibits resonances at 16 and 58 ppm (attributable to residual EtOH) and an additional signal at 50 ppm (unreacted methoxy groups), suggesting an incomplete hydrolysis of the silane precursor.

In all cases the presence of the expected resonances of the specific organic component can be clearly identified (see Scheme S1 with C labelling and Fig. S2a). The behavior of grafted APTES (not shown) is in perfect agreement with our past works (peaks at about 10, 23 and 44 ppm due to C1–C3 of the propyl chain) [41]. The quantitative reaction between the amino groups of APTES and SA used in $SA_{1/2}$-SiO_2 is confirmed by peak area comparison, whereas the C4 chemical shift (δ 174.4 ppm), overlapped with C7 (centered at 178 ppm), proves the formation of the amide bond and the presence of terminal carboxylic

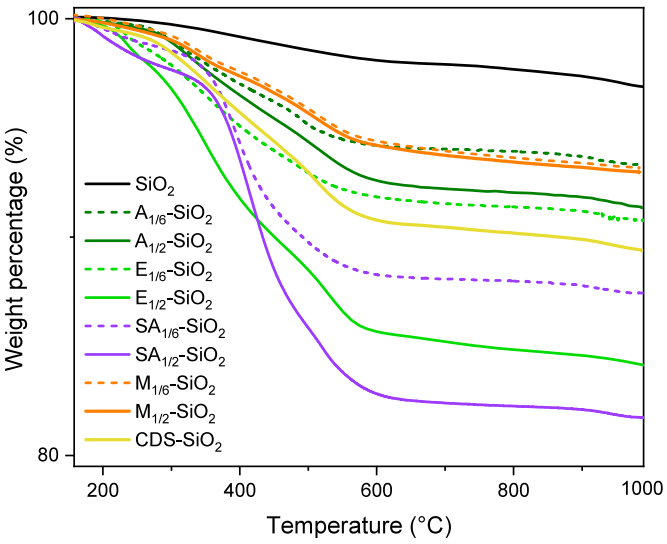

Fig. 3. TGA curves of L-SiO_2 compared to bare SiO_2 between 150 and 1000 °C.

Table 1
Amount of L anchored over SiO_2 calculated from TGA analysis.

Sample	Nominal L:OH molar ratio	Calculated L:OH molar ratio	$\Delta W_{150\text{-}1000\,^\circ C}$ (%)	wt_L (%)	grafting Y (%)	σ (molecules nm^{-2})
SiO_2	-	-	3.3 ± 0.1	-	-	-
A-SiO_2	1/6	1/6	6.6 ± 0.1	4.1 ± 0.1	95	2.4 ± 0.2
	1/2	1/3	9.1 ± 0.2	7.6 ± 0.2	68	5.0 ± 0.2
E-SiO_2	1/6	1/6	9.6 ± 0.2	7.2 ± 0.2	94	2.7 ± 0.2
	1/2	1/3	15.6 ± 0.2	16.4 ± 0.2	83	6.1 ± 0.2
SA-SiO_2	1/6	1/6	12.6 ± 0.3	10.7 ± 0.3	96	2.3 ± 0.2
	1/2	1/3	18.3 ± 0.5	19.9 ± 0.5	65	4.8 ± 0.4
M-SiO_2	1/6	1/6	7.0 ± 0.2	4.6 ± 0.2	91	2.3 ± 0.2
	1/2	1/6	7.2 ± 0.2	4.8 ± 0.2	33	2.4 ± 0.2
CDS-SiO_2	1/2	1/2	10.6 ± 0.3	9.6 ± 0.3	-$(CH_2)_3NH_2$: 68 -CS_2: 17	-$(CH_2)_3NH_2$: 5.0 ± 0.2 -CS_2: 0.85 ± 0.05

Table 2
Amounts of carbon, nitrogen and sulfur measured through CHNS analysis compared to the TGA results. The C/N and C/S molar ratios were calculated using the CHNS results.

Sample	C % (TGA)	C % (CHNS)	N % (TGA)	N% (CHNS)	S% (TGA)	S% (CHNS)	C/N molar ratio	C/S molar ratio
$A_{1/6}$-SiO_2	2.5 ± 0.2	2.7 ± 0.1	1.0 ± 0.2	1.1 ± 0.2	-	-	2.9	-
$A_{1/2}$-SiO_2	4.7 ± 0.2	4.5 ± 0.1	1.8 ± 0.3	1.5 ± 0.2	-	-	3.4	-
$E_{1/6}$-SiO_2	4.3 ± 0.2	4.4 ± 0.2	2.0 ± 0.2	1.9 ± 0.2	-	-	2.7	-
$E_{1/2}$-SiO_2	9.7 ± 0.2	8.9 ± 0.1	4.5 ± 0.3	3.9 ± 0.2	-	-	2.6	-
$SA_{1/6}$-SiO_2	5.7 ± 0.3	6.0 ± 0.2	1.0 ± 0.3	1.1 ± 0.2	-	-	6.4	-
$SA_{1/2}$-SiO_2	10.6 ± 0.5	11.2 ± 0.1	1.8 ± 0.5	2.0 ± 0.2	-	-	6.7	-
$M_{1/6}$-SiO_2	2.2 ± 0.2	2.0 ± 0.2	-	-	1.9 ± 0.2	1.8 ± 0.2	-	3.1
$M_{1/2}$-SiO_2	2.3 ± 0.2	2.3 ± 0.1	-	-	2.0 ± 0.2	1.7 ± 0.2	-	3.4
CDS-SiO_2	5.2 ± 0.3	5.5 ± 0.1	1.9 ± 0.2	1.8 ± 0.1	1.5 ± 0.1	1.8 ± 0.1	3.6	7.9

groups [49]. In CDS-SiO_2 sample, the resonance at 183 ppm assigned to the –CSSH carbon proves the reaction of the amino-bearing silica with carbon disulfide. However, the C3 resonance is composed of two overlapping components centered at 47 and 43 ppm, thus indicating only a partial conversion of the amino group into the dithiocarbamate one. In fact, according to Goubert-Renaudin et al. [50], the α–C resonance of the aminopropyl group appears at 43 ppm, whereas it is shifted at 47 ppm in the case of dithiocarbamate.

The quantification of L on SiO_2 surface was then carried out by TGA analysis, comparing the $\Delta W_{150\text{-}1000\,^\circ C}$ of L-SiO_2 to bare SiO_2 (Fig. 3). The higher weight losses of all L-SiO_2 confirm the effective presence of functionalizing agents onto the silica surface. The amount of grafted L (wt%), the reaction yield of silane grafting (grafting Y, %) and the number of L groups over SiO_2 surface (σ, molecules/nm^2) calculated considering the SiO_2 SSA (160 $m^2\,g^{-1}$) according to Eqs. S4-S6 in the SI are reported in Table 1. The resulting molar ratios between L and SiO_2 surface OH groups (L:OH molar ratio) are calculated for each sample and compared to the nominal values.

For all $L_{1/6}$-SiO_2, the functionalization step proceeds with high reaction yields of grafting (>90 %) and the calculated L:OH molar ratios are equal to the nominal ones. However, by increasing the nominal ratio ($L_{1/2}$-SiO_2), the resulting L:OH molar ratios are lower, suggesting that a maximum level of surface coverage is achieved. In fact, the anchoring of the amino-based ligands in $A_{1/2}$-SiO_2 and $E_{1/2}$-SiO_2 is characterized by lower reaction yields, corresponding to L:OH molar ratios of 1/3 and to 5-6 molecules nm^{-2} for the ligands APTES and EDTMS, respectively.

Regarding the sulfur-based ligands, the lower grafting yield for $M_{1/2}$-SiO_2 (Y = 33 %) indicates that L:OH molar ratio is comparable to that obtained in $M_{1/6}$-SiO_2, and the number of ligands corresponds to almost half of the amino groups available with APTES (2.4 molecules nm^{-2}).

Table 3
Amount of Zn measured for Zn-L-SiO_2 samples through ICP-OES analysis.

Samples	nominal Zn:L (mol:mol)	ICP Zn amount (wt%)	no. of Zn atoms/L-SiO_2 surface (atoms/nm^2)	calculated Zn:L (mol:mol)
Zn-$A_{1/6}$-SiO_2	0.5	1.4 ± 0.1	1.1 ± 0.2	0.46
Zn-$A_{1/2}$-SiO_2	0.5	2.9 ± 0.1	2.4 ± 0.2	0.48
	1	3.1 ± 0.2	2.5 ± 0.2	0.50
	2	3.2 ± 0.2	2.6 ± 0.2	0.52
Zn-$E_{1/6}$-SiO_2	0.5	1.3 ± 0.1	1.1 ± 0.1	0.41
Zn-$E_{1/2}$-SiO_2	0.5	3.5 ± 0.2	3.6 ± 0.2	0.59
	1	5.9 ± 0.2	6.2 ± 0.2	1.02
	2	6.6 ± 0.2	7.1 ± 0.1	1.16
Zn-$SA_{1/6}$-SiO_2	0.5	1.2 ± 0.3	1.0 ± 0.2	0.44
Zn-$SA_{1/2}$-SiO_2	0.5	3.1 ± 0.5	2.7 ± 0.6	0.56
	1	3.5 ± 0.7	3.0 ± 0.7	0.62
	2	3.9 ± 0.7	3.3 ± 0.7	0.68
Zn-$M_{1/6}$-SiO_2	0.5	1.3 ± 0.2	1.1 ± 0.2	0.48
Zn-$M_{1/2}$-SiO_2	0.5	1.5 ± 0.3	1.3 ± 0.2	0.54
	1	1.4 ± 0.4	1.2 ± 0.4	0.50
	2	1.8 ± 0.3	1.5 ± 0.3	0.62
	0.5	1.5 ± 0.1	1.2 ± 0.1	0.24
Zn-CDS-SiO_2	1	1.6 ± 0.2	1.3 ± 0.2	0.26
	2	1.7 ± 0.1	1.3 ± 0.1	0.26

This suggests both that the use of a higher MPTMS amount does not promote a higher functionalization degree and that the hydrolysis and condensation reaction with MPTMS is effectively less efficient as observed by solid state NMR analysis. In the case of CDS-SiO_2, the higher $\Delta W_{150\text{-}1000\,^\circ C}$ compared to that of $A_{1/2}$-SiO_2 is due to $–CS_2$ groups from CDS linked to the terminal amino groups of APTES chains. However, the small difference of $\Delta W_{150\text{-}1000\,^\circ C}$ suggests that the APTES amino groups are only partially substituted by CS_2 groups, in agreement with the previous observation obtained by ^{13}C CPMAS NMR. From the TGA data, it can be estimated that about 17 % of the available $–NH_2$ groups are converted to $–CS_2$, corresponding to about 0.85 $–CS_2$ groups nm^{-2} onto SiO_2 surface. Consequently, both not-converted amino and dithiocarbamate groups are expected to coordinate the metal in CDS-SiO_2.

Similarly, for SA-SiO_2 sample, the presence of $COCH_2CH_2COOH$ groups from SA linked to NH_2 groups of the APTES chains (-$(CH_2)_3NH_2$), is responsible for the higher $\Delta W_{150\text{-}1000\,^\circ C}$ compared to that of A-SiO_2. In this case, the $\Delta W_{150\text{-}1000\,^\circ C}$ increase is consistent with the complete conversion of $–NH_2$ groups into –COOH as indicated also by ^{13}C CPMAS NMR analysis, so that the SA moles correspond to APTES moles in A-SiO_2.

These results are confirmed by CHNS analysis, where the measured percentage of carbon (C%), nitrogen (N%) and sulfur (S%) almost correspond to the amount estimated by TGA (Table 2). Besides, the calculated C/N and C/S molar ratios of A-SiO_2, E-SiO_2 and M-SiO_2 (equal to ~3) are consistent with the ligands used for silica functionalization, where the functional groups are positioned at the end of the isopropyl chain. Whereas the C/N molar ratio of SA-SiO_2 (~7) further validates the almost complete conversion of APTES amino groups with SA, fully supporting the previous observations drawn with both ^{13}C CPMAS experiment and TGA evaluation. Lastly, the overestimated C/S molar ratio of CDS-SiO_2 agrees with the partial substitution of $–NH_2$ groups with CS_2, as already observed by both TGA and SS-NMR.

3.2. *Zn(II) coordination in Zn-L-SiO_2*

After reacting the L-SiO_2 materials with the Zn(II) precursor, the resulting Zn-L-SiO_2 materials were thoroughly characterized to determine the Zn(II) loading, its spatial distribution and the structural features of the most plausible Zn(II) complexes formed on the SiO_2 surface.

First, the amount of Zn(II) in Zn-$L_{1/2}$-SiO_2 and Zn-$L_{1/6}$-SiO_2 prepared by using different Zn:L molar ratios (0,50; 1; 2), was measured by ICP-OES (Table 3) and the number of Zn atoms over SiO_2 surface (atoms/nm^2) calculated considering the $L_{1/2}$-SiO_2 SSA of 107 $m^2\,g^{-1}$ and $L_{1/6}$-SiO_2 (111 $m^2\,g^{-1}$). In the case of $L_{1/6}$-SiO_2 a constant Zn:L molar ratio of 0.50 was used. For all Zn-$L_{1/6}$-SiO_2 samples, the amount of anchored Zn is close to the nominal value and consistent with a Zn:L coordination equal to 0.50. A similar behavior is observed in Zn-$A_{1/2}$-SiO_2, Zn-$SA_{1/2}$-SiO_2 and Zn-$M_{1/2}$-SiO_2, with a calculated Zn:L ratio equal to ~0.50, whatever the nominal Zn:L tested ratios. On the contrary, the Zn(II) loading in Zn-$E_{1/2}$-SiO_2 changes by modifying the Zn: EDTMS ratio, suggesting a modification of the Zn(II) coordination. In fact, at the lowest nominal Zn:L molar ratio (0.50), the resulting calculated ratio is 0.59, while by increasing the nominal Zn:L ratio up to 1 and 2, the measured Zn(II) content correspondently increases, resulting in a Zn:L equal to 1. Finally, in the presence of $–CS_2$ groups in CDS-SiO_2, the calculated Zn(II) loadings at all tested Zn:L nominal ratios (equal to 0.24-0.26) are lower than $A_{1/2}$-SiO_2 used as a precursor. In this case, the experimental Zn:L molar ratio is calculated considering both non-converted $–NH_2$ groups and $–CS_2$ functional groups, whose total number corresponds to that of $A_{1/2}$-SiO_2 (5.0 ± 0.2). These results suggest a lower availability of CDS-SiO_2 to coordinate Zn(II) compared to bare A-SiO_2.

The successful anchoring of Zn(II) onto L-SiO_2 was confirmed also by TEM/EDX analysis. EDX maps of Zn-$E_{1/2}$-SiO_2 as representative sample are presented in Fig. 4, whereas the other materials are provided in Fig. S3. The EDX maps collected for the Zn-L-SiO_2 samples show a

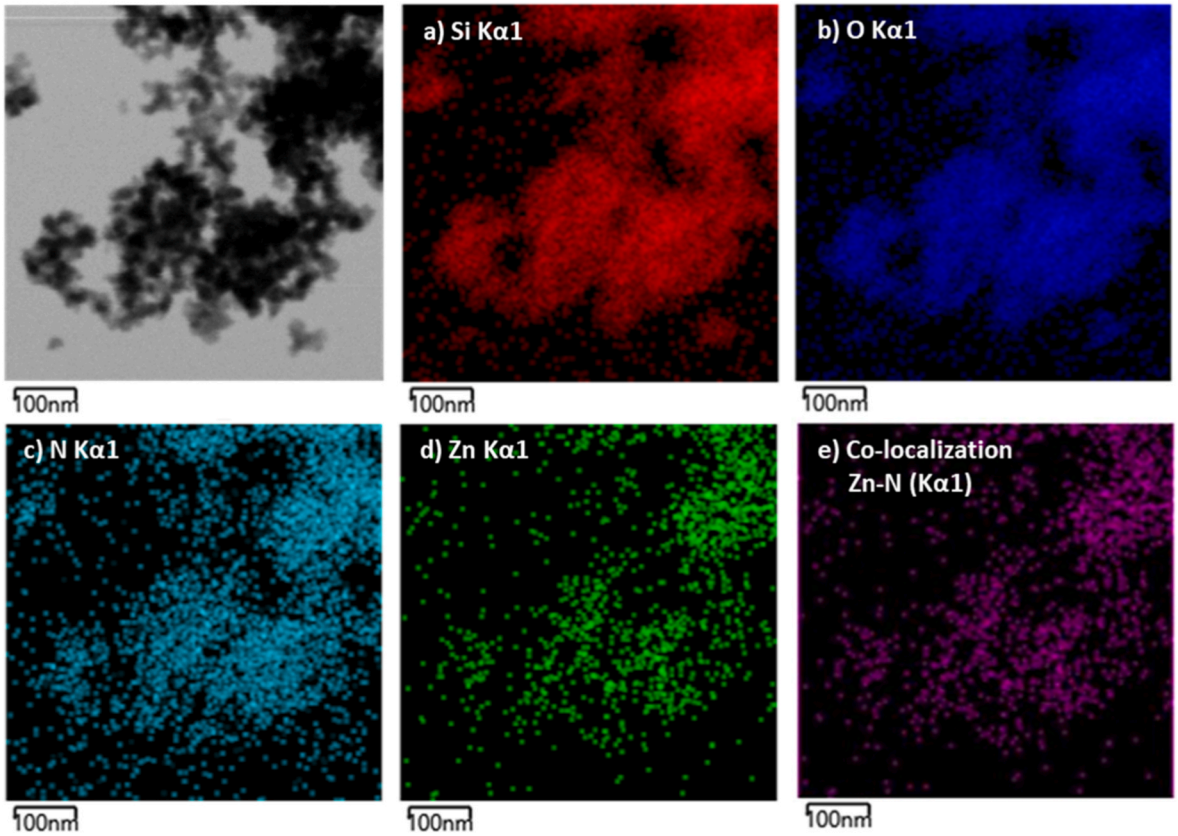

Fig. 4. TEM/EDX maps of Zn-$E_{1/2}$-SiO_2 reported as representative sample. In e) the elemental co-localization image of Zn and N is shown.

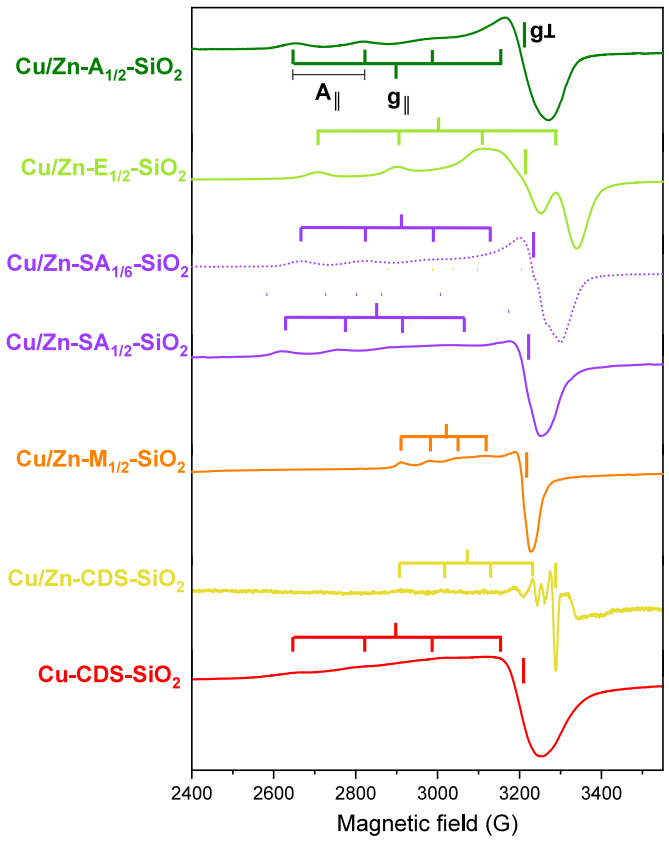

Fig. 5. EPR spectra of Cu/Zn-L-SiO_2 NPs. The position of the magnetic tensor $g_\perp$ and $g_\parallel$ and the hyperfine coupling constant $A_\parallel$ are indicated for each spectrum.

Table 4
Magnetic tensor $g_\perp$ and $g_\parallel$ and the hyperfine coupling constant $A_\parallel$ measured from EPR spectra of Cu/Zn-L-SiO_2.

Sample	$g_\perp$	$g_\parallel$	$A_\parallel$ (G)
Cu/Zn-A-SiO_2	2.06	2.26	185
Cu/Zn-E-SiO_2	2.05	2.19	199
Cu/Zn-$SA_{1/6}$-SiO_2	2.06	2.30	160
Cu/Zn-$SA_{1/2}$-SiO_2	2.06	2.35	140
Cu/Zn-M-SiO_2	2.06	2.16	78
Cu/Zn-CDS-SiO_2	2.03	2.08	110
Cu-CDS-SiO_2	2.06	2.26	185

homogeneous distribution of Zn(II) across the entire surface of the materials for all tested L ligands. This uniform dispersion is consistent with the even distribution observed for the heteroatoms belonging to the terminal groups of L (especially S and N, which are clearly visible in the EDX maps). To further verify this, the degree of overlap between the Zn and N elemental distributions on the material surface was assessed by superimposing the corresponding single-element maps (Fig. 4e). The resulting co-localization confirms the homogeneous distribution of the two elements. Moreover, no Zn(II)-based aggregates were detected, suggesting that ZnO particles do not form during the reaction. This indication is further supported by the XRD patterns, which show no additional peaks attributable to crystalline ZnO particles for all Zn-L-SiO_2 samples (Fig. S4). Altogether, these results suggest that Zn(II) is present mainly as dispersed ionic species rather than as crystalline ZnO domains.

To deepen our understanding of the Zn(II) possible chemical environment, we employed two complementary resonance-based spectroscopic techniques that provided both direct and indirect insights into the nature of the surface Zn(II) complexes. First, EPR spectroscopy was used to assess the ability of the L groups on L-SiO_2 to coordinate isolated metal centers. Although this technique provides only indirect information on the availability of the L ligands and cannot yield direct insight into the Zn(II) coordination environment, it is nevertheless useful for evaluating the uniform distribution of the L groups and the number of the heteroatoms in their terminal functionalities effectively involved for metal binding. To this purpose, EPR spectra of Cu/Zn-L-SiO_2 activators were collected, in which Cu(II) centers act as paramagnetic probes (Cu/Zn molar ratio equal to 1/100, using a Zn:L molar ratio equal to 0.5). The EPR spectra of all Cu/Zn-L-SiO_2 samples display resonance lines attributed to monomeric Cu(II) species in axial symmetry (Fig. 5), confirming the formation of isolated copper centers coordinated to L groups without any metal-metal interactions. This provides an initial indication of the ability of the L groups to bind metal centers on the silica surface. The magnetic tensor values $g_\perp$ and $g_\parallel$ and the hyperfine coupling constant $A_\parallel$ (Table 4) are consistent with tetragonally elongated or square-planar or square pyramidal Cu(II) centers [51] and their values depend on the heteroatoms of the coordinative ligands directly linked to the metal, according to Peisach and Blumberg [52,53].

First, the $g_\perp$ and $g_\parallel$ values along with the $A_\parallel$ value in Cu/Zn-A-SiO_2 are consistent with Cu(II) centers coordinated by two nitrogen and two oxygen atoms [41,52], whereas the lower $g_\parallel$ (2.19) and the higher $A_\parallel$ value (199 G) of Cu/Zn-E-SiO_2 suggest the Cu(II) coordination with four nitrogen atoms in the presence of EDTMS. Regarding the sulfur-based ligands, the lower $g_\parallel$ and $A_\parallel$ values observed for both Cu/Zn-M-SiO_2 and Cu/Zn-CDS-SiO_2 when compared to Cu/Zn-A-SiO_2 are consistent with a sulfur-rich Cu(II) coordination environment [54]. This coordination likely involves either four sulfur atoms or a mixed environment of two sulfur and two nitrogen atoms. Furthermore, the low $A_\parallel$ value of Cu/Zn-M-SiO_2, as well as its high $g_\parallel/A_\parallel$ ratio (274 cm^{-1}), suggests the occurrence of a tetrahedral distortion to the Cu complex [55,56]. To better discriminate between $-CS_2$ and $-NH_2$ groups, both of which are potential ligands in CDS-SiO_2, an additional control experiment was performed. A reference sample prepared in the absence of Zn (Cu-CDS-SiO_2) exhibits the same EPR signal observed in Cu/Zn-A-SiO_2. This suggests that in the presence of an excess of Cu(II), the metal is also coordinated by $-NH_2$ groups; the less intense signal from the sulfur-metal bond is likely obscured by the broader, more dominant APTES-related signal. This observation confirms that both $-NH_2$ and $-CS_2$ ligands are available to coordinate the metal centers. Nevertheless, with the lower amount of Cu(II) used in Cu/Zn-CDS-SiO_2, only the signal related to $-CS_2$ groups is detected, thus suggesting that Cu(II) is first selectively coordinated by these groups and then by the residual APTES molecules. This is in agreement with the previously reported higher chelating efficiency of sulfur-containing ligands towards Cu(II) ions [57].

Lastly, based on the lower $A_\parallel$ and on the higher $g_\parallel$ values, the Cu(II) coordination in Cu/Zn-$SA_{1/2}$-SiO_2 can be described with four oxygen atoms for each Cu(II) center. Interestingly, only in this latter case, the use of different amounts of SA as a ligand for metal coordination led to a modification of the $g_\parallel$ and $A_\parallel$ values: in fact, in Cu/Zn-$SA_{1/6}$-SiO_2 the shift of $g_\parallel$ and the reduction of $A_\parallel$ suggest the possible coordination through one nitrogen and three oxygen or two oxygen and two nitrogen (1N–3O or 2N–2O, respectively) [58], probably involving also the $-NH_2$ group of the ligand chain. This could hinder the coordination of the metal between two adjacent surface ligands, favoring the coordination by a single chain or in-between two SiO_2 NPs. This hypothesis is reasonable by considering that at lower loadings of SA groups, the distance between the anchored ligands strongly increases.

Based on these observations, the EPR results indicate that the use of amino-, sulfur- or carboxyl-containing groups not only enables the coordination of metal centers such as Cu(II) but may also give rise to distinct metal-coordination environments on the silica surface.

To directly elucidate the interaction between the anchored L groups and Zn(II), ^1H and ^{13}C CPMAS NMR spectra of Zn-L-SiO_2 (Fig. S2a and b)

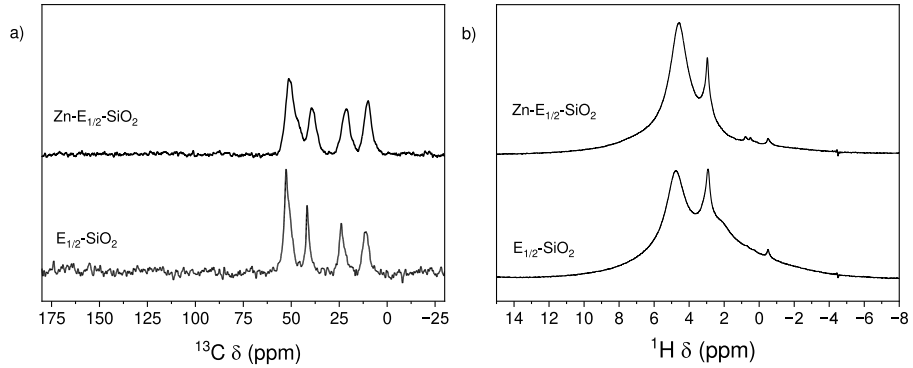

Fig. 6. Representative NMR spectra: (a) ^{13}C CPMAS and (b) ^{1}H MAS spectra recorded for Zn-$E_{1/2}$-SiO_2 shown in comparison to $E_{1/2}$-SiO_2. The complete dataset is provided in the SI.

were recorded and compared to L-SiO_2 and. Solid state NMR experiments were used in a previous wok to confirm Zn(II) complexation with the amino groups of APTES surface ligands [41]. In particular, the presence of a single C2 resonance at 22 ppm in the ^{13}C CPMAS spectrum of Zn-$A_{1/2}$-SiO_2, instead of the two distinct signals observed for the $A_{1/2}$-SiO_2 reference, indicated that the terminal amino groups are predominantly coordinated to Zn(II) rather than interacting with surface silanols. Furthermore, in the ^{1}H MAS spectrum, the disappearance of the sharp peaks at 1.9 and 5.2 ppm, alongside the intensity increase of the bands at 7.3 and 4.6 ppm, further confirmed the Zn(II)-amino groups coordination [59]. Following the same experimental procedure, these analyses were herein applied to the other surface L ligands (all the spectra are reported in Fig. S2a and b). Specifically, the ^{13}C CPMAS NMR spectrum of Zn-$E_{1/2}$-SiO_2 (Fig. 6a, chosen as representative) exhibits a general signal broadening, with the exception of C1, which remains unchanged, likely due to its distance from the amino groups. Furthermore, a 2 ppm upfield shift for C2 and C5, and the appearance of a highfield shoulder for C3/C4 resonances were observed, suggesting that Zn(II) complexation involves both amino groups on the EDTMS organic chains, consistent with previous observations for EDTMS-functionalized silica [60]. This interpretation is further corroborated by the ^{1}H MAS NMR data (Fig. 6b): the broad resonance at ~2 ppm, typical of the -NH_X groups in the parent $E_{1/2}$-SiO_2, disappears upon metal interaction. Despite being poorly resolved, the loss of this signal provides additional evidence that both amine groups are directly engaged in Zn(II) coordination [60].

Regarding the SA-functionalized systems, a downfield shift of the C7 component to 180 ppm in the ^{13}C NMR spectrum of Zn-SA-SiO_2 compared to SA-SiO_2 is clearly visible (Fig. S2a). This suggests the formation of a new bond through the carboxylic groups with Zn(II). While the amide group remains unaffected, the corresponding downfield shifts of C5 and C6 also confirm that metal cations mainly disturb the charge distribution around the nearest methylene groups. Besides, according to the literature, monodentate binding modes are generally more deshielded than bidentate ones, and the higher the chemical shift, the longer the C–O distance [61]. Thus, the ~2 ppm shift could be attributed to the formation of a bidentate chelating coordination, as already reported for various Zn-carboxylates complexes [13,62]. The carboxylate-metal coordination was further validated by analyzing the FTIR stretching frequencies of the carboxylate groups in Zn-SA-SiO_2. Specifically, the coordination mode was determined by comparing the difference ($\Delta\nu_{as\text{-}s}$) between the antisymmetric and symmetric stretching vibrations of the C=O bonds in Zn-$SA_{1/2}$-SiO_2 (ν_{as} and ν_s, respectively) to that of the free anion in solution (Fig. S5a) [63]. For Zn-$SA_{1/2}$-SiO_2, the observed $\Delta\nu_{as\text{-}s} = 133\ cm^{-1}$ is significantly lower than the free succinate anion ($\Delta\nu_{as\text{-}s} = 149\ cm^{-1}$, with ν_{as} at ~ $1558\ cm^{-1}$ and ν_s at ~ $1409\ cm^{-1}$ [64]). According to established spectroscopic criteria [63,65], such a reduction in the $\Delta\nu_{as\text{-}s}$ is characteristic of a bidentate chelating coordination around Zn(II) sites (Fig. S5b). Finally, the corresponding ^{1}H MAS spectrum shows a downfield shift and reduction of the water 4-ppm resonance, together with the disappearance of the broad component centered at about 7 ppm. The latter can reasonably be attributed to –COOH protons [66]; therefore, its disappearance after complexation further supports the Zn(II) interaction with the silane terminal groups.

In the case of MPTMS, evidence of the Zn(II) interaction with terminal –SH groups were provided by the intensity reduction of the C2 and C3 resonances. This indicates a less efficient H→C polarization transfer, which may suggest the partial deprotonation of thiol groups (–SH to $–S^-$) upon Zn(II) complexation. Furthermore, both the slight broadening of these resonances and the formation of a downfield shoulder can be ascribed to metal coordination, which is expected to induce a chemical shift and restrict the mobility of the organic chains. Furthermore, the ^{1}H NMR spectra show marked differences before and after Zn(II) interaction. It is worth noting that the intensity reduction of the main resonance at 4.5 ppm likely reflects a decrease in adsorbed water. This could result from water displacement during complexation, further surface condensation, or variations in the aging and storage conditions of the samples. Lastly, for the Zn-CDS-SiO_2 materials, a decrease in the intensity of both the C4 resonance at 183 ppm and the 47-ppm component of the C3 resonance is observed. The former is attributed to the conversion of –CSSH groups to (–CSS)–Zn species upon metal coordination; the loss of the SH proton significantly reduces the efficiency of H→C cross-polarization. Similarly, the intensity reduction of the 47-ppm component suggests that the H→C polarization transfer for C3 is also affected by the nearby functional groups involved in metal coordination. A possible explanation is that some $–CS_2$ groups may act as bidentate chelating ligands, while others may serve as bridging ligands between two zinc centers. Such coordination modes likely increase the overall rigidity of the organic chains, suppressing the signal intensity at 47 ppm due to altered polarization dynamics. The proposed structural modifications are further supported by the clear changes observed in the ^{1}H spectrum upon Zn^{2+} complexation. The disappearance of the peak at 2.3 ppm and the broadening of the main component at 4.3 ppm are consistent with the loss of the SH proton and with increased chain rigidity following metal coordination. Moreover, the 7.5 ppm resonance, which can be attributed to terminal $–NH_2$ [67], also disappears, supporting the complexation with Zn(II). This picture strengthens the EPR indication of Zn centers coordinated by both N and S terminal groups.

In conclusion, the NMR results provide strong evidence for Zn(II) coordination with the diverse terminal groups of L used for silica functionalization. Interestingly, the combination of ICP-OES, EPR, and NMR data enabled the development of a proposed coordination geometry for the Zn(II) centers (Fig. 7), assuming a likely tetrahedral symmetry in all cases [68].

Consistent with our previous findings, it is suggested that each Zn(II) center in the Zn-A-SiO_2 materials is coordinated by two terminal amino functionalities. Indeed, the constant experimental Zn:L molar ratio of 0.5, coupled with the direct evidence of amine-Zn interactions by NMR,

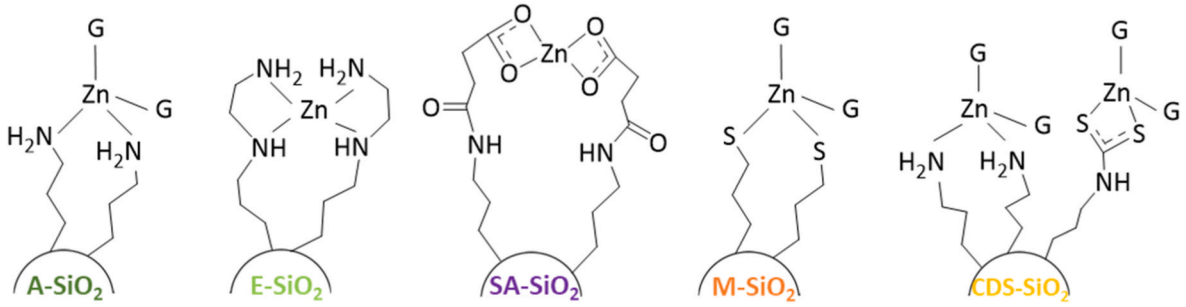

Fig. 7. Suggested Zn(II) coordination in Zn-$L_{1/2}$-SiO_2 (nominal Zn:L molar ratio = 0.5), where G are other groups that coordinate Zn(II) in a tetrahedral structure, as nitrate or hydroxyl groups.

supports a model where the coordination sphere for both Zn-$A_{1/2}$-SiO_2 and Zn-$A_{1/6}$-SiO_2 is composed of two amino groups from the APTES ligands. In this configuration, the remaining two coordination sites on the Zn(II) center are likely occupied by residual nitrate groups or surface hydroxyl species (depicted as G in Fig. 7). Conversely, for both Zn-$E_{1/2}$-SiO_2 and Zn-$E_{1/6}$-SiO_2 (at a nominal Zn:L molar ratio of 0.5) the Zn(II) coordination is proposed to involve two chelating EDTMS molecules, resulting in a coordination sphere where each Zn(II) center is surrounded by four nitrogen atoms from two ethylenediamine molecules. This model is strongly corroborated by EPR spectroscopy, which indicates the availability of both amino groups on the EDTMS chains for metal complexation and further supported by NMR results, which confirm their direct participation in Zn(II) coordination.

Moving to the sulfur-based ligands, the Zn(II) species in Zn-M-SiO_2 samples may be suggested to exhibit a coordination behavior similar to that observed with APTES. In fact, based on ICP-OES results indicating a constant Zn:L molar ratio of 0.5 and supporting NMR evidence on the thiol involvement, the Zn(II) coordination sphere can be reasonably assumed to rely on two terminal –SH groups. As with the APTES system, the remaining two coordination sites could be occupied by residual nitrate groups or hydroxyl species. For Zn-CDS-SiO_2, the combined data show that Zn(II) complexation may occur through both $–CS_2$ and unreacted $–NH_2$ groups on the organic chains. This dual interaction was verified both for Zn(II) and Cu(II) centers, as demonstrated by NMR and EPR, respectively. Thus, a mixed coordination environment model is necessary to accurately describe the metal centers on the functionalized CDS-SiO_2 surface.

Finally, similarly to the EDTMS system, the Zn(II) coordination sphere in Zn-$SA_{1/2}$-SiO_2 can be described as involving four oxygen atoms per Zn(II) center, deriving from two chelating -COO^- groups, as strongly suggested by both NMR and FTIR direct evidence. However, EPR data also revealed that reducing the amount of SA on the surface of SiO_2 (from 1/2 to 1/6) shifts the Cu(II) coordination toward a 2N–2O or 1N–3O environment. To determine if a similar effect occurs for the Zn (II) centers, FTIR analysis was conducted on Zn-$SA_{1/6}$-SiO_2 (Fig. S5a). The spectrum shows a shift in the ν_{as} peak toward higher wavenumbers compared to Zn-$SA_{1/2}$-SiO_2. Specifically, a sharp peak at 1570 cm^{-1} becomes predominant, corresponding to $\Delta\nu_{as\text{-}s} = 155\ cm^{-1}$. This increase in the $\Delta\nu_{as\text{-}s}$ value suggests that at lower ligand loadings, the Zn–COOH coordination shifts from bidentate chelating mode toward a bridging or monodentate coordination mode (Figure Sb), as observed for Cu(II).

To summarize, different ligands were successfully used to anchor Zn (II) centers on SiO_2 NPs as demonstrated by ICP-OES and TEM/EDX analysis. EPR and NMR spectroscopies proved instrumental in elucidating the structural features of the metal complexes formed on the SiO_2 surface (Fig. 7). Briefly, Zn(II) centers are possibly coordinated through two nitrogen and sulfur atoms in the presence of APTES and MPTMS, respectively, leaving the other two positions of the tetrahedral geometry available for nitrates or hydroxyl group. On the contrary, a chelate structure around the Zn(II) centers with four oxygen and nitrogen atoms can be reasonable supposed by using SA and EDTMS, respectively. Finally, in the case of CDS, both $–NH_2$ and $–CS_2$ groups are available for the Zn(II) coordination thus leading to a mixed coordination geometry.

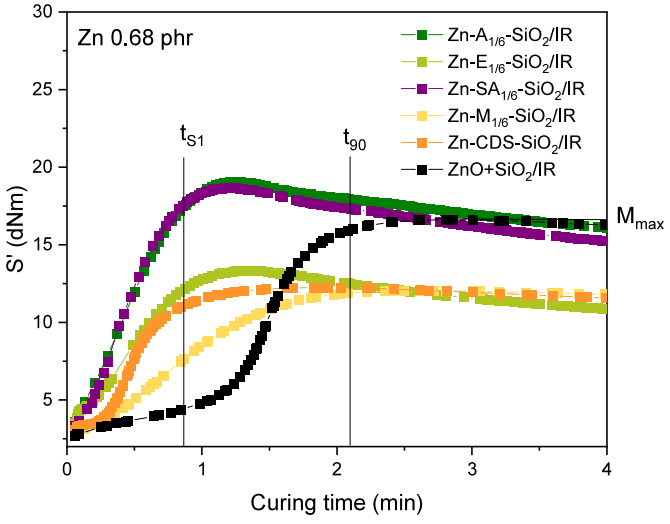

Fig. 8. Vulcanization curves of Zn-$L_{1/6}$-SiO_2/IR NCs compared to ZnO + SiO_2/IR NCs (Zn content = 0.68 phr). The maximum torque (M_{max}), the scorch time (t_{s1}) and the optimum curing time (t_{90}) are indicated for ZnO + SiO_2/IR.

3.3. Curing of elastomeric NCs with Zn-L-SiO_2

To evaluate the possible effect of the different metal coordination on the zinc reactivity as curing activator, as well as on the filler networking, IR NCs were prepared by using Zn-$L_{1/6}$-SiO_2 and Zn-$L_{1/2}$-SiO_2 (Zn:L molar ratios equal to 0.5) both as curing activator and reinforcing filler. Thus, the role of the Zn(II) coordination onto the surface of SiO_2 NPs was tested in the curing process by determining the availability of the metal centers towards the other curing agents. First, the vulcanization curves of Zn-$L_{1/6}$-SiO_2/IR at 170 °C (torque values S' vs curing time) were recorded and compared to that of the conventional reference sample ZnO + SiO_2/IR NC at equal Zn content (0.68 phr, Fig. 8).

For all IR NCs the increase of the torque modulus S' is connected to the higher viscosity of the vulcanized NCs due to the sulfur cross-link formation between the polymer chains. By comparing the vulcanization curves of Zn-$L_{1/6}$-SiO_2/IR with that of ZnO + SiO_2/IR, a reduced scorch time is evident (t_{s1}, Fig. 8, Table S1 and Fig. S6), that is the time required to start the cross-linking process in the matrix after the initial interaction between the curing agents and the formation of the active sulfurating agents [4]. Analogously, the optimum curing time (t_{90}, time to reach the 90 % of the maximum curing torque, M_{max}, Fig. 8 and Table S1) is decreased compared to that of ZnO + SiO_2/IR. These phenomena can be related to the higher availability of the Zn centers in Zn-L-SiO_2 to react with the curing agents compared to the zinc centers

obtained from the microcrystalline ZnO lattice in the conventional reference process [41]. This strongly reduces the time required for the reaction with the curing agents in the first vulcanization steps and prompts the cross-links formation in the rubber matrix in the subsequent curing process.

Interestingly, the use of different L ligands led also to a different vulcanization efficiency in terms of M_{max} (Fig. 8) and curing rate indices (CRI, Table S1): in fact, in the presence of Zn-$A_{1/6}$-SiO_2 and Zn-$SA_{1/6}$-SiO_2 a slightly higher M_{max} value and higher CRI values are obtained compared to ZnO + SiO_2/IR, consistent with a good reactivity of the Zn centers during the curing process. However, by using the sulfur-based ligands in Zn-$M_{1/6}$-SiO_2 and Zn-CDS-SiO_2 a reduction of the M_{max} and CRI values is observed. This phenomenon is particularly interesting in the case of Zn-CDS-SiO_2/IR, in which the presence of a mixed coordination geometry around the zinc centers, that involves both amino- and sulfur-based ligands, partially reduces its efficiency compared to Zn-A-SiO_2, that was used as a precursor while maintaining a good overall reaction kinetics. The observed variations in performance can be rationalized by examining the stability constants of the Zn(II) complexes formed with the various ligands. Since oxygen, nitrogen, and sulfur serve as the coordinating donor atoms, the resulting complexes exhibit distinct degrees of thermodynamic stability, a phenomenon described by the Irving-Williams series for divalent metal ions of the first transition series [69,70]. The slope and progression of this series can be considered at least in part as a result of the hard and soft characteristics of both the metal center and the donor atoms. In this framework, amino- and carboxyl-based ligands, possessing harder donor atoms (N and O), maintain the Zn(II) center in a more Lewis-acidic state. The resulting electronic environment around Zn(II) probably facilitates its interaction with the curing agents. Conversely, sulfur-based ligands promote enhanced soft-soft interactions, leading to significantly higher complex stability, which ultimately reduces their efficiency. This effect is particularly evident in the case of Zn-CDS-SiO_2, where the replacement of an amino group with a sulfur-based moiety increases the stability of the zinc complex, as reported by Sigel et al. [71], thereby resulting in a marked reduction in the curing efficiency compared to Zn-A-SiO_2/IR reference.

To better analyze the surface Zn(II)-complex activity in the vulcanization process of IR NCs, also Zn-$L_{1/2}$-SiO_2 samples were tested to increase the Zn content in the resulting NCs up to 1.50 phr. These NCs were compared to a reference ZnO + SiO_2/IR sample at the same silica and zinc content (43.0 and 1.50 phr, respectively). For these tests, only the amino- and carboxyl-based samples (i.e. Zn-$A_{1/2}$-SiO_2, Zn-$E_{1/2}$-SiO_2 and Zn-$SA_{1/2}$-SiO_2) were used because of the low functionalization degrees obtained with the sulfur-based ligands, as well as their low curing performances.

As observed before, reduced scorch times (t_{s1}) and faster reaction kinetics (i.e. lower t_{90} and higher CRI) are highlighted with all Zn-$L_{1/2}$-SiO_2/IR than ZnO + SiO_2/IR (Fig. 9a and Table 5), confirming the higher availability of the single Zn(II) centers to react with the curing agents. Noteworthy, a higher t_{s1} is observed for both Zn-$E_{1/2}$-SiO_2/IR and Zn-$SA_{1/2}$-SiO_2/IR compared to Zn-$A_{1/2}$-SiO_2/IR. To further elucidate this trend, it must be considered that the geometric arrangement of the Zn(II) sites plays a pivotal role in defining vulcanization kinetics. As previously described in Ref. [41], the coordination of each Zn(II) center by only two APTES units in Zn-A-SiO_2, complemented by two labile ligands (such as hydroxyl or nitrate groups), ensures high accessibility for the curing agents. In contrast, as illustrated in Fig. 7, the introduction of chelating ligands (SA and EDTMS) induces a steric shielding effect around the metal center, creating a closed configuration that could effectively explain the prolonged scorch time observed in these systems. This structure-activity relationship suggests that while electronic properties dictate the overall curing efficiency, the coordination geometry is the primary tool for controlling the scorch time.

On the other hand, a significant improvement of the vulcanization efficiency is evident by the increase of M_{max} compared to ZnO + SiO_2/IR, as well as the elastic moduli G' (Fig. 9b and Table 5), especially for Zn-$A_{1/2}$-SiO_2/IR. Surprisingly, the curing efficiency of Zn-$SA_{1/2}$-SiO_2/IR and Zn-$E_{1/2}$-SiO_2/IR are almost comparable with similar M_{max}, differently from the case at lower Zn content. This can be connected to the strong chelating coordination of the Zn(II) single sites due to the ligands with four nitrogen or oxygen atoms, respectively, that are responsible for an almost equivalent reactivity.

To confirm the higher cross-linking efficiency achieved by Zn-$L_{1/2}$-SiO_2, the cross-linking densities of Zn-$L_{1/2}$-SiO_2/IR were measured through swelling experiments in toluene and calculated by following Eqs. S7-S8 in the SI. According to the higher M_{max} measured during the vulcanization process, Zn-$A_{1/2}$-SiO_2, Zn-$E_{1/2}$-SiO_2 and Zn-$SA_{1/2}$-SiO_2 promote higher ν_{sw} values (Table S2) than the reference ZnO + SiO_2/IR.

Finally, Fig. 10 summarizes semi-quantitatively the discussed correlations among the zinc coordination on the silica surface obtained by using different L coordinative groups and the properties of the resulting IR NCs. In particular, both t_{s1} and ΔM were modulated by tuning the coordination of the Zn(II) single sites of the curing activators, thus leading to different vulcanization performances. This strongly support that a fine tailoring of the structural and electronic of Zn(II) allows targeted adjustments to the reactivity of rubber curing activators.

4. Conclusion

This work focused on the preparation of Zn-L-SiO_2 curing activators by using five different silane functionalizing agents to modify the surface of commercial SiO_2 NPs and tailor the coordination sphere of anchored Zn(II) sites. The ligands differ in terms of the heteroatoms involved in the Zn(II) coordination (N, O, S) and on their ability to promote Zn(II) complexes with different geometrical features. To this purpose, amino-based (APTES and EDTMS), carboxyl-based (SA) and sulfur-based (MPTMS and CDS) groups were selected as suitable L for Zn-L-SiO_2

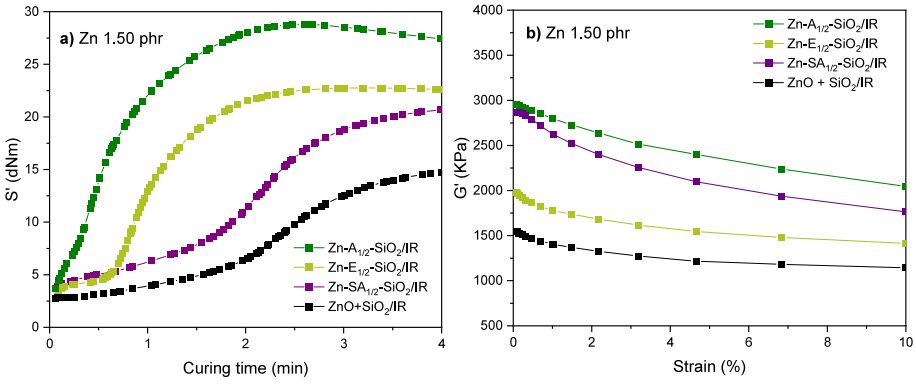

Fig. 9. a) Vulcanization curves and b) elastic modulus G' (0-10 % strain) of Zn-$L_{1/2}$-SiO_2/IR NCs compared to ZnO + SiO_2/IR NCs (Zn content = 1.50 phr).

Table 5
Vulcanization Parameters and Mechanical Properties of Zn-$L_{1/2}$-SiO_2/IR and ZnO + SiO_2/IR (1.50 phr) NCs: M_{min} = Minimum Torque; M_{max} = Maximum Torque; ΔM = torque increase calculated as $M_{max} - M_{min}$; t_{S1} = Scorch Time; t_{90} = Time to Achieve 90 % of M_{max}; G'_0 = Elastic Modulus at Low Strain (0.1 %); $G'_{10\,\%}$ = Elastic Modulus at 10 % Strain. The curing rate index (CRI) was calculated as $100/(t_{90} - tS_1)$.

Zn content (phr)	Sample	M_{min} (dNm)	t_{s1} (min)	M_{max} (dNm)	ΔM (dNm)	t_{90} (min)	G'_0 (KPa)	$G'_{10\,\%}$ (KPa)	CRI
1.50	Zn-$A_{1/2}$-SiO_2/IR	3.8	0.1	28.8	25.0	1.6	2958	2045	67
	Zn-$E_{1/2}$-SiO_2/IR	3.1	0.5	22.8	19.7	1.9	1980	1414	71
	Zn-$SA_{1/2}$-SiO_2/IR	3.7	0.8	21.0	17.3	3.0	2869	1765	45
	ZnO + SiO_2/IR	2.8	0.8	15.3	12.5	3.4	1550	1144	38

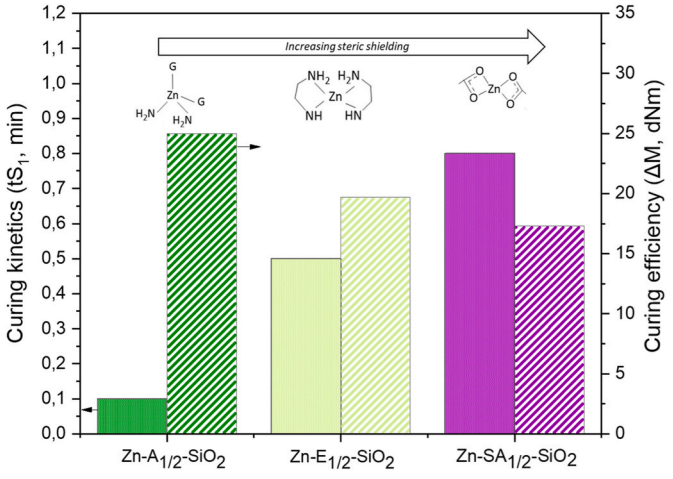

Fig. 10. t_{s1} and ΔM values of IR NCs as a function of the coordination of Zn(II) curing activators.

synthesis.

All the ligands were successfully anchored onto SiO_2 surface, as demonstrated by FTIR, SS-NMR, TGA and elemental analyses. The good ability to form metal complexes and the structural features of the Zn(II) sites were deeply investigated by EPR and SS-NMR, respectively. The good efficiencies obtained in the curing process for all Zn-L-SiO_2 materials demonstrated that the grafting method ensures a homogeneous dispersion of Zn(II) as isolated sites through the terminal functional groups, maximizing the atom economy of the activator compared to traditional bulk ZnO. Besides, the main advantage of this functionalization strategy lies in its high degree of tunability, as the selection of specific ligands directly allowed modulation of the curing efficiency and kinetics of IR NCs. A fundamental relationship was identified between ligand donor properties, Zn(II) complex stability and resulting efficiencies: only the nitrogen and oxygen donors lead to competitive Zn(II) reactivity in the curing process, whereas the soft sulfur donors promote the formation of stable Zn(II) complexes that hinder its reaction with the curing agents. In fact, both amino-based and carboxyl-based Zn(II) complexes showed high curing efficiencies and led to vulcanized IR NCs with good mechanical properties. Furthermore, it was demonstrated that the use of chelating ligands (SA and EDTMS) enabled superior control over the scorch delay. While the monodentate ligands (APTES and MPTMS) provide an open environment and highly accessible Zn(II) sites, the chelation effect induces a steric shielding effect over Zn(II). This offers a strategic advantage by extending the processing safety window during rubber compounding without compromising the final cross-linking density.

Although the current synthesis requires further optimization to ensure its viability for industrial scale-up, these results clearly demonstrate that the reactivity of the activator is governed by the electronic and geometric nature of its coordination sphere. This study thus provides a generalizable roadmap for the fine-tailoring of metal-based activators, enabling the precise modulation of rubber vulcanization through rational ligand selection.

CRediT authorship contribution statement

Silvia Mostoni: Conceptualization, Investigation, Supervision, Writing – original draft, Writing – review & editing. **Paola Milana:** Investigation, Writing – original draft, Writing – review & editing. **Lorenzo Alberti:** Investigation, Writing – review & editing. **Massimiliano D'Arienzo:** Resources, Writing – review & editing. **Emanuela Callone:** Data curation, Investigation, Methodology, Validation, Writing – review & editing. **Sandra Dirè:** Investigation, Methodology, Resources, Writing – review & editing. **Antonio Susanna:** Resources, Visualization. **Raffaella Donetti:** Resources, Visualization. **Barbara Di Credico:** Resources, Writing – review & editing. **Roberto Scotti:** Conceptualization, Resources, Supervision, Writing – review & editing.

Declaration of competing interest

The authors declare that they have no known competing financial interests or personal relationships that could have appeared to influence the work reported in this paper.

Acknowledgements

PM and LA thank CORIMAV (Consortium for the Research of Advanced Materials between Pirelli and the Milano Bicocca University) for its support within the Doctoral Program.

Appendix A. Supplementary data

Supplementary data to this article can be found online at https://doi.org/10.1016/j.mtchem.2026.103770.

Data availability

Data will be made available on request.

References

[1] A.Y. Coran, Vulcanization, in: Sci. Technol. Rubber, Academic Press, 1994, pp. 339–385.
[2] V. Ducháček, A. Kuta, P. Přibyl, Efficiency of metal activators of accelerated sulfur vulcanization, J. Appl. Polym. Sci. 47 (1993) 743–746, https://doi.org/10.1002/app.1993.070470418.
[3] G. Heideman, R.N. Datta, J.W.M. Noordermeer, B. Van Baarle, Influence of zinc oxide during different stages of sulfur vulcanization. elucidated by model compound studies, J. Appl. Polym. Sci. 95 (2005) 1388–1404, https://doi.org/10.1002/app.21364.
[4] G. Heideman, R.N. Datta, J.W.M. Noordermeer, B. van Baarle, Activators in accelerated sulfur vulcanization, Rubber Chem. Technol. 77 (2004) 512–541, https://doi.org/10.5254/1.3547834.
[5] M.M. Coleman, J.R. Shelton, J.L. Koenig, Sulfur vulcanization of hydrocarbon diene elastomers, Ind. Eng. Chem. Prod. Res. Dev. 13 (1974) 154–166.
[6] P.J. Nieuwenhuizen, Zinc accelerator complexes. Versatile homogeneous catalysts in sulfur vulcanization, Appl. Catal. Gen. 207 (2001) 55–68, https://doi.org/10.1016/S0926-860X(00)00613-X.
[7] M.R. Krejsa, J.L. Koenig, A review of sulfur crosslinking fundamentals for accelerated and unaccelerated vulcanization, Rubber Chem. Technol. 66 (1993) 376–410, https://doi.org/10.5254/1.3538317.
[8] P. Ghosh, S. Katare, P. Patkar, E. Al, Sulfur vulcanization of natural rubber for benzothiazole accelerated formulations : from reaction mechanisms to a rational kinetic model, Rubber Chem. Technol. 76 (2003) 592–693, https://doi.org/10.5254/1.3547762.

[9] H. Wang, Q. Xu, K. Liu, B. Shi, L. Zhang, J. Tang, C. Li, J. Shen, H. Jiang, Elucidation of the reactive process involving ZnO crystal facets and stearic acid during rubber vulcanization, Appl. Surf. Sci. 710 (2025) 163889, https://doi.org/10.1016/j.apsusc.2025.163889.
[10] Y. Ikeda, Y. Yasuda, T. Ohashi, H. Yokohama, S. Minoda, H. Kobayashi, T. Honma, Dinuclear bridging bidentate zinc/stearate complex in sulfur cross-linking of rubber, Macromolecules 48 (2015) 462–475, https://doi.org/10.1021/ma502063m.
[11] Z.B. Hou, W.L. Xie, G.X. Liu, S. Liao, M.C. Luo, Design of vulcanization intermediates with low steric hindrance contributing to vulcanization network formation, ACS Appl. Polym. Mater. 5 (2023) 4509–4516, https://doi.org/10.1021/acsapm.3c00624.
[12] A. Susanna, M. D'Arienzo, B. Di Credico, L. Giannini, T. Hanel, R. Grandori, F. Morazzoni, S. Mostoni, C. Santambrogio, R. Scotti, Catalytic effect of ZnO anchored silica nanoparticles on rubber vulcanization and cross-link formation, Eur. Polym. J. 93 (2017) 63–74, https://doi.org/10.1016/j.eurpolymj.2017.05.029.
[13] S. Mostoni, P. Milana, M. D'Arienzo, S. Dirè, E. Callone, C. Cepek, S. Rubini, A. Farooq, C. Canevali, B. Di Credico, R. Scotti, Studying stearic acid interaction with ZnO/SiO2 nanoparticles with tailored morphology and surface features: a benchmark for better designing efficient ZnO-based curing activators, Ceram. Int. 49 (2023) 24312–24321, https://doi.org/10.1016/j.ceramint.2022.12.013.
[14] Y. Ikeda, K. Miyaji, Y. Sakaki, T. Ohashi, H. Kobayashi, Ingenious material design of the vulcanization of isoprene rubber: electron-transfer and dispersion effects, Organometallics 41 (2022) 1942–1959, https://doi.org/10.1021/acs.organomet.2c00139.
[15] F. Shi, X. Li, Y. Bai, L. Li, M. Pu, L. Liu, M. Lei, Mechanism of the zinc dithiocarbamate-activated rubber vulcanization process: a density functional theory study, ACS Appl. Polym. Mater. 3 (2021) 5188–5196, https://doi.org/10.1021/acsapm.1c00902.
[16] S. Wagner, T. Hüffer, P. Klöckner, M. Wehrhahn, T. Hofmann, T. Reemtsma, Tire wear particles in the aquatic environment - a review on generation, analysis, occurrence, fate and effects, Water Res. 139 (2018) 83–100, https://doi.org/10.1016/j.watres.2018.03.051.
[17] L.F. Magni, L.N. Castro, A.E. Rendina, Evaluation of heavy metal contamination levels in river sediments and their risk to human health in urban areas: a case study in the Matanza-Riachuelo Basin, Argentina, Environ. Res. 197 (2021) 110979, https://doi.org/10.1016/j.envres.2021.110979.
[18] T. Hennequin, L. van Vlimmeren, S. Mostoni, F.R. Pomilla, R. Scotti, C. Stauch, M. K. van der Hulst, M.A.J. Huijbregts, R. van Zelm, Environmental impact prediction of a new tire vulcanization activator, ACS Sustain. Chem. Eng. 12 (2024) 6102–6110, https://doi.org/10.1021/acssuschemeng.3c06640.
[19] B. Kim, S. Kim, R. Kim, Y. Heo, J. Jo, S. Ahn, S. Jeon, S.H. Woo, S. Lee, J.J. Kim, Y. J. Kim, T.H. Shin, J.W. Park, W.S. Cho, Comparative toxicity of tire wear particle leachates: zinc as a key toxicant affecting development and motility in zebrafish larvae, J. Hazard Mater. 499 (2025) 140296, https://doi.org/10.1016/j.jhazmat.2025.140296.
[20] Z.A. Ganie, S. Guchhait, M. Talib, A. Choudhary, G.K. Darbha, Investigating the sorption of zinc-oxide nanoparticles on tire-wear particles and their toxic effects on Chlorella vulgaris: insights from toxicological models and physiological analysis, J. Hazard Mater. 483 (2025) 136648, https://doi.org/10.1016/j.jhazmat.2024.136648.
[21] M. Tavakoli, P. Peyzari, F. Tamaddon, B. Zare-Banadkouki, A novel zinc complex for rubber vulcanization: enhanced mechanical properties and reduced environmental impact through ZnO substitution, Polym. Eng. Sci. 65 (2025) 2699–2713, https://doi.org/10.1002/pen.27176.
[22] C. Nakason, P. Nuthong, A. Kaesaman, Transforming waste cooking oil into zinc soap: a sustainable approach to multifunctional additives for enhancing natural rubber composites, J. Polym. Res. 32 (2025) 1–17, https://doi.org/10.1007/s10965-025-04392-2.
[23] M. Maciejewska, A. Sowińska, A. Grocholewicz, Zinc complexes with 1,3-diketones as activators for sulfur vulcanization of styrene-butadiene elastomer filled with carbon black, Materials 14 (2021), https://doi.org/10.3390/ma14143804.
[24] A. Zanchet, F.D.B. de Sousa, J.S. Crespo, C.H. Scuracchio, Activator from sugar cane as a green alternative to conventional vulcanization additives, J. Clean. Prod. 174 (2018) 437–446, https://doi.org/10.1016/j.jclepro.2017.10.329.
[25] G. Heideman, J.W.M. Noordermeer, R.N. Datta, B. Van Baarle, Effect of zinc complexes as activator for sulfur vulcanization in various rubbers, Rubber Chem. Technol. 78 (2005) 245–257, https://doi.org/10.5254/1.3547881.
[26] M. Przybyszewska, M. Zaborski, B. Jakubowski, J. Zawadiak, Zinc chelates as new activators for sulphur vulcanization of acrylonitrile-butadiene elastomer, Express Polym. Lett. 3 (2009) 256–266, https://doi.org/10.3144/expresspolymlett.2009.32.
[27] H.K. Abgorg, S.O. Movahed, The effect of nano-zinc oxide on the mechanical properties of the cured ethylene-propylene-diene monomer rubber with a semi-efficient vulcanisation system, Plast, Rubber Compos. 53 (2024) 168–177, https://doi.org/10.1177/14658011241273533.
[28] A.K. B, S. Sahoo, M. Maiti, A. Ganguly, J.J. George, Effect of zinc oxide nanoparticles as cure activator on the properties of natural rubber and nitrile rubber, J. Appl. Polym. Sci. 105 (2007) 2407–2415, https://doi.org/10.1002/app.26296.
[29] E.E. Elemike, F.C. Ibeh, W. Ivwurie, D.C. Onwudiwe, Effect of green synthesized zinc oxide nanoparticles as cure activator on the mechanical properties of natural rubber vulcanizate, Chem. Pap. 77 (2023) 7717–7724, https://doi.org/10.1007/s11696-023-03072-z.
[30] D.M. Bieliński, K. Klajn, T. Gozdek, R. Kruszyński, M. Świątkowski, Influence of n-zno morphology on sulfur crosslinking and properties of styrene-butadiene rubber vulcanizates, Polymers 13 (2021) 1–15, https://doi.org/10.3390/polym13071040. Basel.
[31] X. Qin, H. Xu, G. Zhang, J. Wang, Y. Zhao, Z. Wang, T. Tan, M.R. Bockstaller, L. Zhang, K. Matyjaszewski, Z. Wang, Enhancing the performance of rubber with nano ZnO as activators, ACS Appl. Mater. Interfaces 12 (2020) 48007–48015, https://doi.org/10.1021/acsami.0c15114.
[32] D. Akin Sahbaz, E. Goksu, Potential use of ZnO anchored boron industrial waste microparticles as a novel eco-friendly activator in cis-polybutadiene/natural rubber composites, Solid State Sci. 163 (2025), https://doi.org/10.1016/j.solidstatesciences.2025.107884.
[33] A. Susanna, L. Armelao, E. Callone, S. Dirè, M. D'Arienzo, B. Di Credico, L. Giannini, T. Hanel, F. Morazzoni, R. Scotti, ZnO nanoparticles anchored to silica filler. A curing accelerator for isoprene rubber composites, Chem. Eng. J. 275 (2015) 245–252, https://doi.org/10.1016/j.cej.2015.04.017.
[34] P. Wetchakama, S. Boopasiri, P. Sae-Oui, P. Poosimma, C. Siriwong, Preparation and application of a zinc oxide/microcrystalline cellulose composite as a cure activator in comparison with a commercial zinc oxide composite, ACS Omega 10 (2025) 5953–5962, https://doi.org/10.1021/acsomega.4c09909.
[35] M.N. Alam, P. Potiyaraj, Precipitated nano zinc hydroxide on the silica surface as an alternative cure activator in the vulcanization of natural rubber, Rubber Chem. Technol. 90 (2017) 714–727, https://doi.org/10.5254/rct.18.83701.
[36] Z. Yang, Y. Huang, Y. Xiong, A functional modified graphene oxide/nanodiamond/nano zinc oxide composite for excellent vulcanization properties of natural rubber, RSC Adv. 10 (2020) 41857–41870, https://doi.org/10.1039/d0ra07404g.
[37] Y. Li, J. Wu, Q. Zhang, F. Dong, Y. Xiong, Novel architecture of ZnO nanobundles grown on porous silica as high performance vulcanization accelerators that reinforce rubber composites, Ind. Eng. Chem. Res. 59 (2020) 4493–4503, https://doi.org/10.1021/acs.iecr.9b06235.
[38] M.M. Hossen, M.S. Hasan, M.R.I. Sardar, J. bin Haider, Mottakin, K. Tammeveski, P. Atanassov, State-of-the-art and developmental trends in platinum group metal-free cathode catalyst for anion exchange membrane fuel cell (AEMFC), Appl. Catal. B Environ. 325 (2023) 121733, https://doi.org/10.1016/j.apcatb.2022.121733.
[39] X. Yang, A. Wang, B. Qiao, J.U.N. Li, Single-atom catalysts : a new frontier in heterogeneous catalysis, Acc. Chem. Res. 46 (2013), https://doi.org/10.1021/ar300361m&2013.
[40] N. Cheng, L. Zhang, K. Doyle-Davis, X. Sun, Single-Atom Catalysts: from Design to Application, Springer Singapore, 2019, https://doi.org/10.1007/s41918-019-00050-6.
[41] S. Mostoni, M. D'Arienzo, B. Di Credico, L. Armelao, M. Rancan, S. Dirè, E. Callone, R. Donetti, A. Susanna, R. Scotti, Design of a Zn single-site curing activator for a more sustainable sulfur cross-link formation in rubber, Ind. Eng. Chem. Res. 60 (2021) 10180–10192, https://doi.org/10.1021/acs.iecr.1c01580.
[42] S. Wenderoth, P. Milana, T. Zimmermann, M. Deues, M. Oppmann, J. Prieschl, S. Mostoni, R. Scotti, S. Wintzheimer, K. Mandel, Assembly of zinc-single-site-containing silica nanoparticles to supraparticle powders with destructibility to serve as filler and vulcanization activator in rubbers, Part. Part. Syst. Char. 41 (2024) 1–10, https://doi.org/10.1002/ppsc.202300161.
[43] S. Mostoni, P. Milana, C. Marano, L. Conzatti, M. Mauri, M. D'Arienzo, B. Di Credico, R. Simonutti, P. Stagnaro, R. Scotti, Localizing the cross-links distribution in elastomeric composites by tailoring the morphology of the curing activator, Compos. Sci. Technol. 230 (2022) 109780, https://doi.org/10.1016/j.compscitech.2022.109780.
[44] R. Ellerbrock, M. Stein, J. Schaller, Comparing amorphous silica, short-range-ordered silicates and silicic acid species by FTIR, Sci. Rep. 12 (2022) 1–8, https://doi.org/10.1038/s41598-022-15882-4.
[45] S.G. Coombs, S. Khodjaniyazova, F.V. Bright, Exploiting the 3-Aminopropyltriethoxysilane (APTES) autocatalytic nature to create bioconjugated microarrays on hydrogen-passivated porous silicon, Talanta 177 (2018) 26–33, https://doi.org/10.1016/j.talanta.2017.09.038.
[46] W. Xue-Ying, W. Ya-Zhen, D. Yu-Tao, L. Tian-Yu, Z. Li-Wu, Preparation and thermal decomposition kinetics of novel silane coupling agent with mercapto group, J. Nanomater. 2019 (2019), https://doi.org/10.1155/2019/6089065.
[47] K. Stawicka, M. Gierada, J. Gajewska, F. Tielens, M. Ziolek, The importance of residual water for the reactivity of MPTMS with silica on the example of SBA-15, Appl. Surf. Sci. 513 (2020) 145802, https://doi.org/10.1016/j.apsusc.2020.145802.
[48] P. Lakshmanan, S. Thirumaran, S. Ciattini, Synthesis, spectral and structural studies on NiS2PN and NiS2P2 chromophores and use of Ni(II) dithiocarbamate to synthesize nickel sulfide and nickel oxide for photodegradation of dyes, J. Mol. Struct. 1220 (2020) 128704, https://doi.org/10.1016/j.molstruc.2020.128704.
[49] Z. Söyler, K.N. Onwukamike, S. Grelier, E. Grau, H. Cramail, M.A.R. Meier, Sustainable succinylation of cellulose in a CO2-based switchable solvent and subsequent passerini 3-CR and ugi 4-CR modification, Green Chem. 20 (2018) 214–224, https://doi.org/10.1039/c7gc02577g.
[50] S. Goubert-Renaudin, F. Gaslain, C. Marichal, B. Lebeau, R. Schneider, A. Walcarius, Synthesis of dithiocarbamate-functionalized mesoporous silica-based materials: interest of one-step grafting, New J. Chem. 33 (2009) 528–537, https://doi.org/10.1039/b811780b.
[51] E. Garribba, G. Micera, The determination of the geometry of Cu(II) complexes. An EPR spectroscopy experiment, J. Chem. Educ. 83 (2006) 1229–1232, https://doi.org/10.1021/ed083p1229.
[52] J. Peisach, W.E. Blumberg, Structural implications derived from the analysis of electron paramagnetic resonance spectra of natural and artificial copper proteins,

Arch. Biochem. Biophys. 165 (1974) 691–708, https://doi.org/10.1016/0003-9861(74)90298-7.
[53] B. Bennett, J.M. Kowalski, EPR Methods for Biological Cu(Ii): L-Band CW and NARS Dedication. This Chapter is Dedicated to Graeme R. Hanson, a Valued Friend and Colleague, who Passed away on February 24th, 2015, first ed., Elsevier Inc., 2015 https://doi.org/10.1016/bs.mie.2015.06.030.
[54] B.G. Malmström, T. Vänngård, Electron spin resonance of copper proteins and some model complexes, J. Mol. Biol. 2 (1960) 118–124, https://doi.org/10.1016/S0022-2836(60)80034-4.
[55] B.K. Maiti, L.B. Maia, A.J. Moro, J.C. Lima, C.M. Cordas, I. Moura, J.J.G. Moura, Unusual reduction mechanism of copper in cysteine-rich environment, Inorg. Chem. 57 (2018) 8078–8088, https://doi.org/10.1021/acs.inorgchem.8b00121.
[56] S.K. Hoffmann, J. Goslar, S. Lijewski, A. Zalewska, EPR and ESE of CuS4 complex in Cu(dmit)2: G-factor and hyperfine splitting correlation in tetrahedral Cu-sulfur complexes, J. Magn. Reson. 236 (2013) 7–14, https://doi.org/10.1016/j.jmr.2013.08.009.
[57] S. Cobianco, A. Lezzi, R. Scotti, Spectroscopic study of Cu(II)-complexes of chelating resins containing nitrogen and sulfur atoms in the chelating groups, React. Funct. Polym. 43 (2000) 7–16, https://doi.org/10.1016/S1381-5148(98)00077-7.
[58] R. Punis, A. Zoleo, Cu(II)-binder complexes in azurite and malachite pictorial mixtures: an EPR study, Microchem. J. 200 (2024) 110303, https://doi.org/10.1016/j.microc.2024.110303.
[59] S.H. Kim, O.H. Han, J.K. Kim, K.H. Lee, Multinuclear solid-state NMR investigation of nanoporous silica prepared by sol-gel polymerization using sodium silicate, Bull. Kor. Chem. Soc. 32 (2011) 3644–3649, https://doi.org/10.5012/bkcs.2011.32.10.3644.
[60] T. Baskaran, R. Kumaravel, J. Christopher, T.G. Ajithkumar, A. Sakthivel, An environmentally friendly route for grafting of molybdenum carbonyl onto a diaminosilane-modified SBA-15 molecular sieve and its catalytic behaviour in olefin epoxidation, New J. Chem. 39 (2015) 3758–3764, https://doi.org/10.1039/c4nj02402h.
[61] C. Leroy, T.X. Métro, I. Hung, Z. Gan, C. Gervais, D. Laurencin, From operando raman mechanochemistry to “nMR crystallography”: understanding the structures and interconversion of Zn-Terephthalate networks using selective 17O-Labeling, Chem. Mater. 34 (2022) 2292–2312, https://doi.org/10.1021/acs.chemmater.1c04132.
[62] M. Kalinowska, R. Świsłocka, W. Lewandowski, Zn(II), Cd(II) and Hg(I) complexes of cinnamic acid: FT-IR, FT-Raman, 1H and 13C NMR studies, J. Mol. Struct. 993 (2011) 404–409, https://doi.org/10.1016/j.molstruc.2011.01.063.
[63] G.B. Deacon, J. Philips, Relationships between carbon-oxygen stretching frequencies of carboxylato complexes and the type of carboxylate coordination, Coord. Chem. Rev. 33 (1980) 227–250, https://doi.org/10.1016/S0010-8545(00)80455-5.
[64] S.J. Hug, D. Bahnemann, Infrared spectra of oxalate, malonate and succinate adsorbed on the aqueous surface of rutile, anatase and lepidocrocite measured with in situ ATR-FTIR, J. Electron. Spectrosc. Relat. Phenom. 150 (2006) 208–219, https://doi.org/10.1016/j.elspec.2005.05.006.
[65] C.C.R. Sutton, G. Da Silva, G.V. Franks, Modeling the IR spectra of aqueous metal carboxylate complexes: correlation between bonding geometry and stretching mode wavenumber shifts, Chem. Eur J. 21 (2015) 6801–6805, https://doi.org/10.1002/chem.201406516.
[66] G. Wu, Y. Dai, I. Hung, Z. Gan, V. Terskikh, 1H/17O chemical shift waves in carboxyl-bridged hydrogen bond networks in organic solids, J. Phys. Chem. A 128 (2024) 4288–4296, https://doi.org/10.1021/acs.jpca.4c01866.
[67] N.J. Daniecki, N.V. Costantini, G.M. Sametz, N.J. Zondlo, A dataset of simple 1-D and 2-D NMR spectra of peptides, including all encoded amino acids, for introductory instruction in protein biomolecular NMR spectroscopy, ChemRxiv (2025), https://doi.org/10.26434/chemrxiv-2024-zww4n-v2.
[68] R.R. Roe, Y.-P. Pang, Zinc's exclusive tetrahedral coordination governed by its electronic structure, J. Mol. Model. 5 (1999) 134–140, https://doi.org/10.1007/s008940050113.
[69] H. Irving, R.J.P. Williams, The stability of transition metal complexes, J. Chem. Soc. 637 (1953).
[70] J. Li, M. Du, Z. Wu, X. Zhang, W. Xue, H. Huang, C. Zhong, Engineering single-atom sites with the Irving Williams series for the simultaneous Co-photocatalytic CO2 reduction and CH3CHO oxidation, Angew. Chem. Int. Ed. 63 (2024) e202407975, https://doi.org/10.1002/anie.202407975.
[71] H. Sigel, D.B. McCoemick, On the discriminating behavior of metal ions and ligands with regard to their biological significance, Acc. Chem. Res. 3 (1970) 201–208, https://doi.org/10.1021/ar50030a004.